Role of Mg doping in the structural, optical, and electrical characteristics of ZnO-based DSSCs

İsmail POLAT[1],[*], **Salih YILMAZ**[2], **Murat TOMAKİN**[3], **Emin BACAKSIZ**[4]
[1]Department of Energy Systems Engineering, Faculty of Technology, Karadeniz Technical University,
Trabzon, Turkey
[2]Department of Materials Engineering, Faculty of Engineering and Natural Sciences,
Adana Science and Technology University, Adana, Turkey
[3]Department of Physics, Faculty of Arts and Sciences, Recep Tayyip Erdoğan University, Rize, Turkey
[4]Department of Physics, Faculty of Sciences, Karadeniz Technical University, Trabzon, Turkey

Abstract: ZnO- and Mg-doped ZnO samples are prepared by spray pyrolysis on conducting glass substrates to fabricate ZnO-based dye-sensitized solar cells (DSSCs). Influences of Mg-doping content on the power conversion efficiencies of ZnO-based DSSCs are investigated. X-ray diffraction results show that all the samples exhibit a hexagonal wurtzite structure. Scanning electron microscopy data indicate that the ZnO sample has uniform rods with 1 μm diameter. With respect to ZnO, the band gap value of 4 at.% Mg-doped ZnO samples improves to the value of 3.27 eV and a further increase in Mg level up to 6 at.% gives rise to a decline in the band gap value of 3.22 eV. Photoluminescence measurements illustrate that intensities of the ultraviolet peak and a red luminescence peak take their maximum values for 4 at.% Mg doping. From solar cell performance measurements, the best power conversion efficiency of 0.08% is obtained for the doping amount of 4 at.% Mg.

Key words: Mg-doped ZnO, rods, spray pyrolysis, dye-sensitized solar cells

1. Introduction

Dye-sensitized solar cells (DSSCs), as introduced by O'Regan and Gratzel [1], are promising power devices due to their low cost and moderate efficiency compared to conventional solar cells [2]. DSSCs based on TiO$_2$ have been extensively studied and their efficiency reaches as high as 11% [3,4]. ZnO material with a wide-band gap semiconductor is considered as an alternative to TiO$_2$ for the photoanode in DSSCs. The attractions of the using ZnO materials stem from its unique properties such as wide bandgap ($\sim$3.37 eV), high charge carrier (electron) mobility, large exciton binding energy (60 meV), controllability of structure and property, simplicity of the synthesis process [5–7], and having various applications [8].

ZnO can be grown by a number of techniques including chemical bath deposition (CBD) [9], magnetron sputtering [10], solid-phase synthesis [11], thermal evaporation [12], epitaxial growth [13], and spray pyrolysis (SP) [14]. SP has many advantages over the other methods because it is one of the simplest and ensures low-cost production as well as a large area film coating. Various elements such as F, Cu, Ag, and Mg can be also easily doped into the ZnO matrix by using this technique [15–20]. Therefore, physical properties of the

---

*Correspondence: ismlpolat@yahoo.com

ZnO material including resistivity, surface morphology, photocatalytic activity, and band gap can be altered by appropriate doping [15–20]. It can be also seen from the literature that metal doping (Al, Na, Mg) into ZnO has an important effect to improve the photovoltaic parameters of ZnO-based DSSCs. For example, Yun et al. investigated the use of an Al-doped ZnO nanorod produced on conducting substrates as photoanode in DSSCs. They reported that the power conversion efficiencies were improved by Al doping [21]. Polat fabricated DSSCs consisting of Na-doped ZnO nanorods on fluorine-doped tin oxide (FTO) substrates as photoanodes and he found that the power conversion efficiency increased from 0.114% to 0.220% by doping of 2 at.% Na [22]. Additionally, Mg-doped ZnO thin films were synthesized by Raj et al. on FTO substrates to fabricate ZnO-based DSSCs. They investigated the influence of doping concentration varying from 0 to 20 at.% with an increment of 5 at.% on the performance of the solar cell. They found that efficiency of the solar cell improved up to 5 at.% and a further increase caused a reduction in power conversion efficiency [23].

The purpose of our study is to produce undoped and Mg-doped ZnO-based DSSCs with high power conversion efficiency. Although the influence of Mg-doping on the performance of ZnO-based DSSCs was previously reported in the literature, to the best of our knowledge, there is no work using SP to prepare undoped and Mg-doped ZnO samples as photoanodes in ZnO-based DSSCs. The work also investigates the effects of Mg-doping on the structural, optical, and electrical characteristics of ZnO samples. Additionally, the study establishes a correlation between morphological and electrical properties of undoped and Mg-doped ZnO samples in order to clarify the reason for the variation in the power conversion efficiency values.

2. Experimental procedure

In the present study, zinc acetate dihydrate $(Zn(OOCCH_3)_2.2H_2O)$, zinc chloride anhydrous $(ZnCl_2)$, and magnesium chloride hexahydrate $(MgCl_2.6H_2O)$ were used as precursors. Prior to the deposition of undoped and Mg-doped ZnO samples, a thin layer of a ZnO seed layer was coated to achieve well-aligned rod arrays on substrates. The substrates were cleaned ultrasonically with soap, ethanol, and distilled water for 10 min, consecutively. The growth process of the ZnO seed layer can be found in our previous work [22]. After this procedure, Mg-doped ZnO samples $(Zn_{1-x}Mg_xO:$ x = 0.0, 0.02, 0.04, 0.06) were grown by SP at different doping levels. To obtain ZnO and Mg-doped ZnO samples, $ZnCl_2$ solution with a concentration of 0.1 M for ZnO sample and mixtures of appropriate amount of $ZnCl_2$ and $MgCl_2.6H_2O$ equimolar (0.1 M) solutions for various doping samples were prepared in a mixture of deionized water and ethanol in the ratio of 2:3 and then were sprayed on preseeded substrates at 400 °C. During the growth, the plate of substrates was rotated at 10 rev/min and it was seen that uniform coverage with good adhesion to the substrate surface was obtained for all the samples.

The grown undoped and Mg-doped ZnO samples onto FTO substrates were used as photoanodes. They were immersed in 0.5 mM solution of N719 dye in absolute ethanol for 24 h in the dark at room temperature (RT). A Pt counter electrode was obtained by spin coating on FTO substrate using Pt solution (Platisol T, Solaronix) and then annealed at 450 °C for 10 min. The fabrication of DSSCs was completed by injecting electrolyte solution (Iodolyte AN-50, Solaronix) between two electrodes. The schematic diagram of the fabricated device is presented in Figure 1.

X-ray diffraction (XRD) patterns were studied by diffractometer with CuK_α irradiation. The micrographs of the samples were taken by scanning electron microscopy (SEM). Chemical compositions were obtained using energy dispersive X-ray spectrometer (EDS). The optical properties of samples at RT were measured by

spectrophotometer. Photoluminescence spectra with an excitation wavelength of 320 nm at RT were obtained. The I-V curves were measured by a source-meter under the solar simulator with AM 1.5D filter and it was operated by the light output of 100 mW/cm^2.
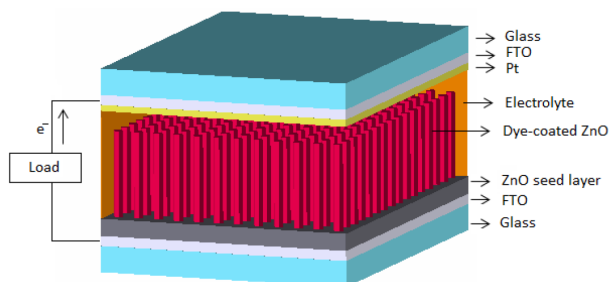

Figure 1. Schematic diagram of the fabricated ZnO-based DSSCs.

3. Results and discussion

Figures 2a–2d show the XRD data for undoped, 2 at.%, 4 at.%, and 6 at.% Mg-doped ZnO samples, respectively. The XRD pattern of ZnO rods given in Figure 2a shows some reflection planes of (100), (002), (101), (102), (110), (103), and (112) of ZnO with the preferred orientation along the c-axis, implying a hexagonal wurtzite structure (JCPDS card no: 36-1451). Besides ZnO peaks, some diffraction peaks at (110), (101), (200), (211), (220), (310), and (301) planes corresponding to SnO$_2$ (JCPDS card no: 36-1451), coming from the FTO substrates, are also seen in the pattern. The 2 at.% Mg-doped ZnO sample exhibits a similar XRD pattern except for an increase in the (101) peak intensity compared to the (101) peak of the undoped sample, which is almost an indication of random orientation. As for 4 at.% Mg doping, the intensity of the (103) diffraction plane increases although the preferred orientation is conserved in the [002] direction. However, for the 6 at.% Mg-doped ZnO sample, the peak intensity of (002) decreases significantly, which causes a change in the preferred orientation from (002) to (101). The reason for the reduction in the peak intensity of (002) may be attributed to the deterioration of the crystal quality upon the incorporation of more Mg atoms in the structure. The Mg-doped ZnO samples do not include any metallic Mg or secondary phase like MgO in the patterns, suggesting that Mg atoms successfully dissolve in the ZnO matrix even up to 6 at.% Mg-doping amount without forming any impurity phases. Compared to the ZnO, it was seen that diffraction peaks of the 6 at.% Mg-doped ZnO sample shift to higher angle values, which show a decline in the lattice parameter values of a and c. It was found that ZnO rods have a and c lattice parameter values of 3.24 Å and 5.19 Å, respectively. These values in turn decrease 5.18 Å and 3.23 Å for the 6 at.% Mg-doped ZnO sample. The reduction in both lattice parameters can be explained by the substitutional incorporation of Mg^{2+} ions at sites of Zn^{2+} ions because the ionic radius of Mg^{2+} ions (0.74 Å) is lower than that of Zn^{2+} ions (0.66 Å) [24].

Figures 3a–3d and 4a–4d indicate the top view and 60° tilted side view images of undoped, 2 at.%, 4 at.%, and 6 at.% Mg-doped ZnO samples, respectively. As seen in Figures 3a and 4a, the ZnO sample is composed of very compact rod morphology with hexagons that are perpendicular to the substrate surface. The distribution of rods is almost homogeneous in the sample and the diameters of the rods are nearly 1 μm. After 2 at.% Mg doping, as illustrated in Figures 3b and 4b, the surface morphology of rods significantly changes. Dense polyhedral rod morphology with an irregular structure forms though some rods with hexagons also appear in the sample. This may originate from the competition between the crystal plane growth of ZnO, resulting
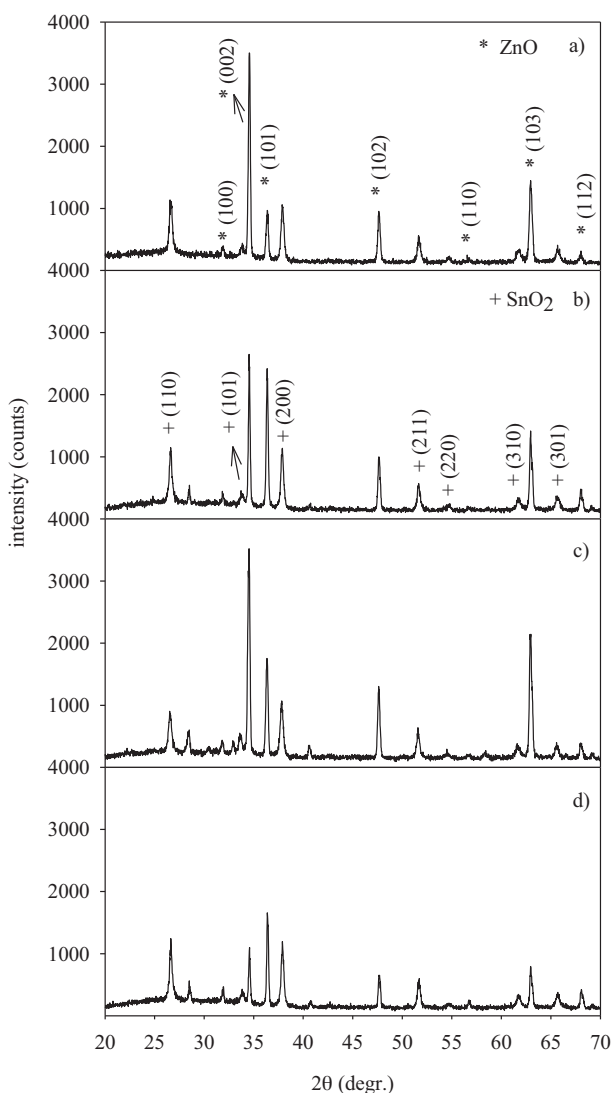
Figure 2. X-ray diffraction patterns of (a) undoped, (b) 2 at.%, (c) 4 at.%, and (d) 6 at.% Mg-doped ZnO samples.

in more random orientation, which is in good agreement with the XRD data (Figure 2b). Figures 3c and 4c show the surface morphology of the 4 at.% Mg-doped ZnO sample. The sample consists of the irregular shaped rods. Some of the rods longitudinally break up into thin slabs and the others resemble hollow hexagons. Furthermore, the 6 at.% Mg-doped ZnO sample (Figures 3d and 4d) includes many small thin rods with very uniform distribution. It is also seen that the ends of the rods transform into rounded structures with a smooth surface morphology and the diameters of these rods are smaller with respect to the other samples. Compared to ZnO rods, the reason for the significant change seen in the surface morphology of all the Mg-doped ZnO samples may be the substitutional incorporation of Mg atoms (as discussed in the XRD results). It is known that the Pauli electronegativity of Mg (1.31) is lower than that of Zn (1.65), which indicates that Mg atoms are more chemically reactive than Zn atoms, causing variation in the growth regime of ZnO including Mg atoms. Therefore, the surface morphology substantially changes [25].

The analyses of elemental homogeneity and chemical composition of the undoped, 2 at.%, 4 at.%, and
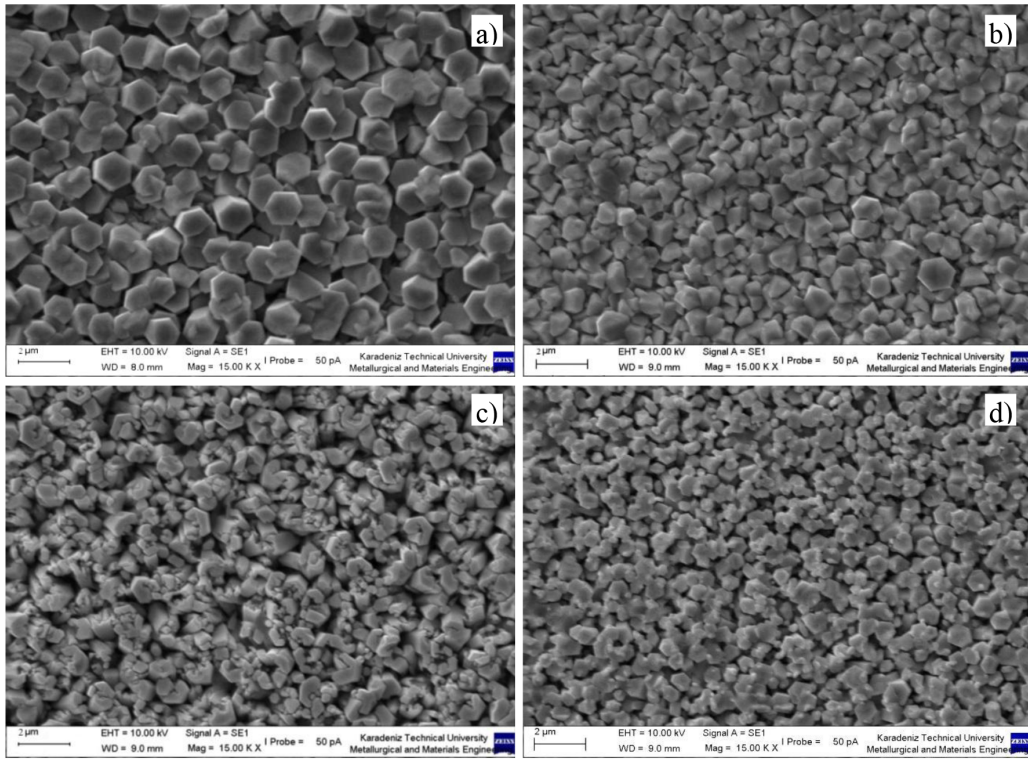
Figure 3. SEM images of (a) undoped, (b) 2 at.%, (c) 4 at.%, and (d) 6 at.% Mg-doped ZnO samples.
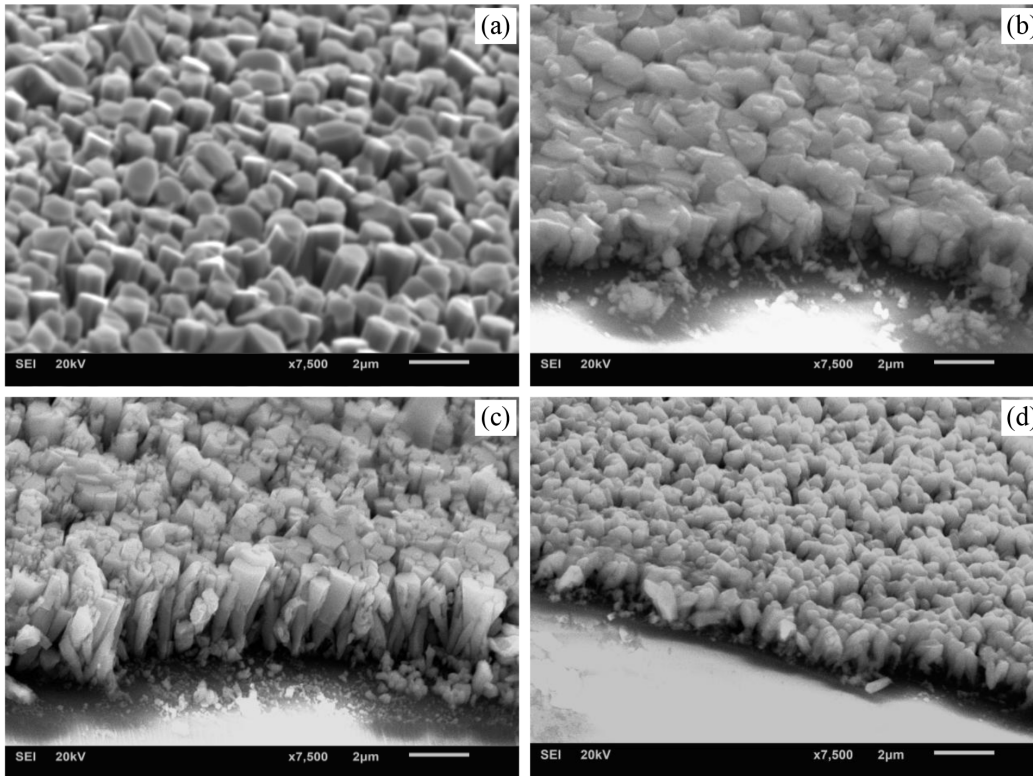

Figure 4. Side view SEM images with 60° tilt of (a) undoped, (b) 2 at.% Mg, (c) 4 at.% Mg, and 6 at.% Mg-doped ZnO samples.

164

6 at.% Mg-doped samples are performed by EDS measurements and the results are presented in Figure 5 and Table 1, respectively. Figure 5a displays the EDS elemental mapping of 2 at.% Mg-doped ZnO sample, which includes O, Mg, and Zn. It is also seen from Figures 5c and 5d that O, Mg, and Zn are uniformly distributed in the sample. Table 1 lists the actual compositions of Zn, O, and Mg in undoped and Mg-doped ZnO samples. As can be seen from the table, the presence of Mg atoms in Mg-doped ZnO samples indicates that Mg atoms are incorporated into the host matrix of ZnO. It is also seen that the actual Mg-doping content in ZnO increases with the increase in nominal Mg content. However, it is found that the actual doping values of Mg atoms are lower than those of nominal ones, which is most probably due to the nonuniform distribution of Mg atoms in the host structure.
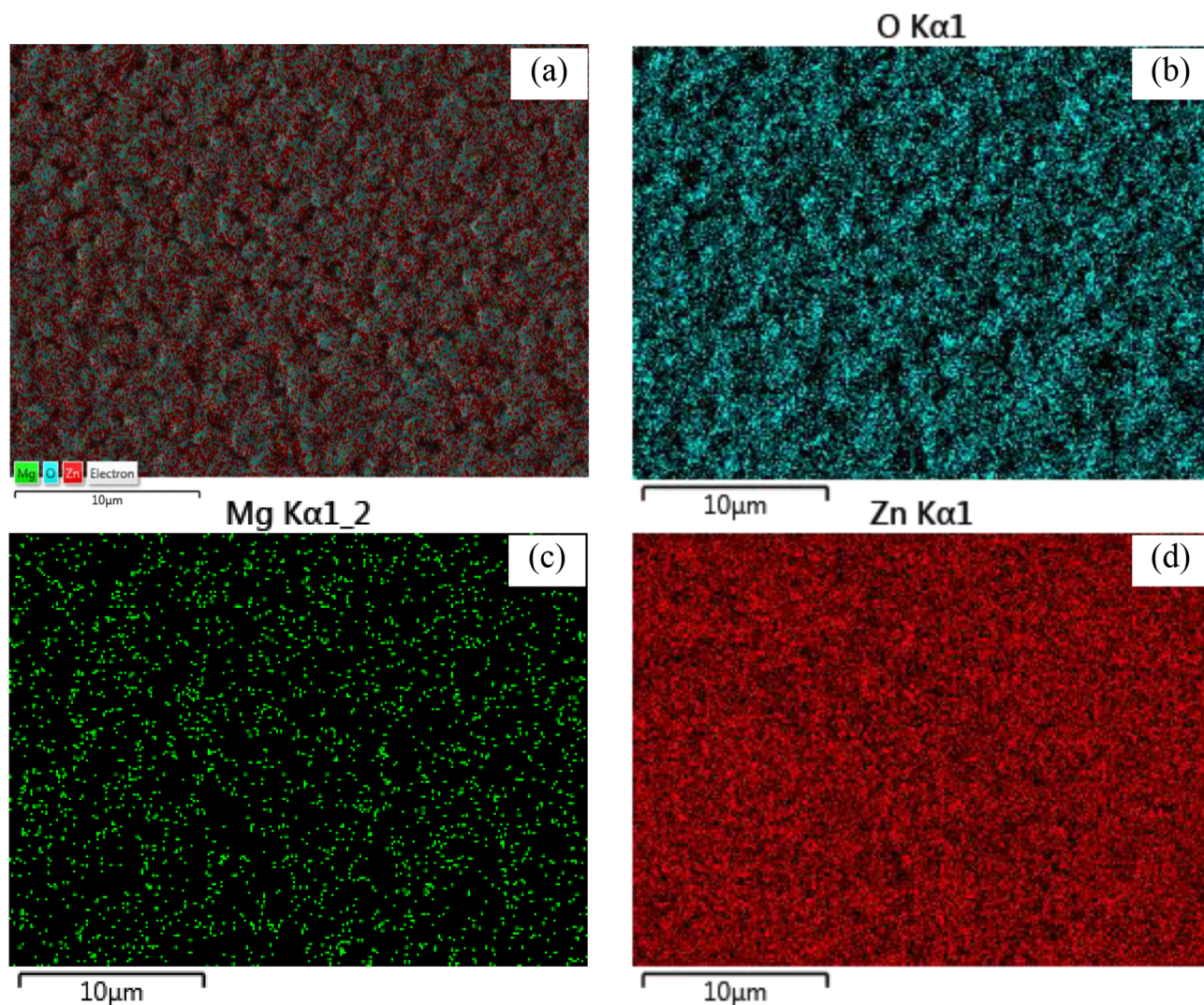
Figure 5. (a) A SEM image and EDS elemental mapping of O (b), Mg (c), and Zn (d) elements of 2 at.% Mg-doped ZnO sample.

Optical transparency of the samples is examined by the transmittance measurements and the results are given in Figure 6. ZnO rods exhibit a transmittance of nearly 50% at the wavelength range of 550–900 nm. The low transmittance is ascribed to the nonplanar surface of the rods, causing the light to scatter from the surface

Table 1. Actual Zn, O, and/or Mg atomic concentrations in undoped, 2 at.%, 4 at.%, and 6 at.% Mg-doped ZnO samples.

Samples	Zn	O	Mg
ZnO	52.23	47.77	-
2 at.% Mg-doped ZnO	51.26	48.30	0.44
4 at.% Mg-doped ZnO	48.64	50.69	0.67
6 at.% Mg-doped ZnO	55.44	43.48	1.08

of the sample [26]. Compared to ZnO rods, the transmittance values of Mg-doped ZnO samples are low. The decline in transmittance after Mg doping may be explained by the following points: (i) A degradation in crystal quality is observed especially after 6 at.% Mg-doping as indicated in XRD data, which leads to the creation of a more defected structure that gives rise to the decline in transmission. (ii) As shown in the SEM results, Mg doping causes an increase in surface roughness of the 2 at.% and 4 at.% Mg-doped ZnO samples, which brings about scattering of the light from the surface, concluding in lower transparency. In previous work reported by our group we observed a similar decreasing behavior in transmittance data of ZnO nanorods synthesized by CBD upon Mg doping [24]. As seen in Figure 6, the absorption edge shifts to the shorter wavelength range with the increase in Mg-doping amount. The band gap values (E_g) of the samples are calculated using Tauc's relationship [27] and the resultant data are illustrated in Figure 7, associated with undoped, 2 at.%, 4 at.%, and 6 at.% Mg-doped ZnO samples. As seen from the graph, ZnO rods have an E_g value of 3.16 eV. For 2 at.% and 4 at.% Mg-doping concentrations, the band gap values of ZnO are calculated to be 3.22 eV and 3.27 eV, respectively, which imply that a lower amount of Mg doping significantly increases the band gap value of ZnO. It can be also stated that there are many reported papers on the increase in the optical band gap of ZnO material after Mg doping in the literature and our results are consistent with them [28,29]. This enhancement in the optical band gap may be explained as follows. It is well known that the band gap value of MgO (7.80 eV) is much larger than that of ZnO bulk material (3.37 eV). Therefore, successful incorporation of Mg atoms into the ZnO host matrix leads to a wider band gap for ZnO since the electronegativity of Mg (1.23) is lower than that of Zn (1.66), which gives rise to an increase in the probability of formation of points defects like V_{Zn}, Zn_i, and O_i. Compared with ZnO rods, 2 at.% and 4 at.% Mg-doped ZnO samples include more V_{Zn}, Zn_i, and O_i defects (will be discussed in the PL section) as seen in Figure 8, which shows an enhancement in the band gap of ZnO [30]. However, with a further increase in the doping amount up to 6 at.% Mg, the band gap value of ZnO decreases to 3.22 eV, which could be attributed to the reduction in the population of V_o defects as displayed in Figure 8. A similar decline in the band gap value of ZnO nanocrystals with 2 at.% Mg-doping nanocrystals was also observed by Abed et al. They found that the band gap value increased up to 2 at.% Mg-doping and a further increase in the doping amount caused a reduction in the optical band gap values. They attributed this to the creation of new electronic states in the band gap [31].

Figure 8 shows the RTPL spectra of undoped, 2 at.%, 4 at.%, and 6 at.% Mg-doped ZnO samples. It is seen that undoped and Mg-doped ZnO samples exhibit a UV peak located at 379 nm (3.27 eV), corresponding to band gap values of ZnO and ZnO:Mg samples, which can be ascribed to the direct recombination of free electrons/holes [32]. Compared with ZnO rods, the intensity of the UV peak enhances with the increase in Mg content up to 4 at.%, which is an indication of improved crystalline quality. A further increase in the Mg-doping amount up to 6 at.% causes a reduction in the UV peak, which is due to degradation of the crystal quality, which is also in good agreement with the XRD data. This may be explained by the lattice distortion created by
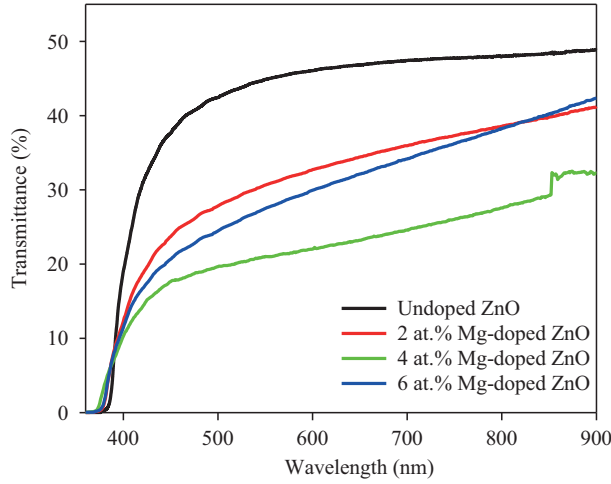
Figure 6. Transmittance spectra of undoped, 2 at.%, 4 at.%, and 6 at.% Mg-doped ZnO samples.
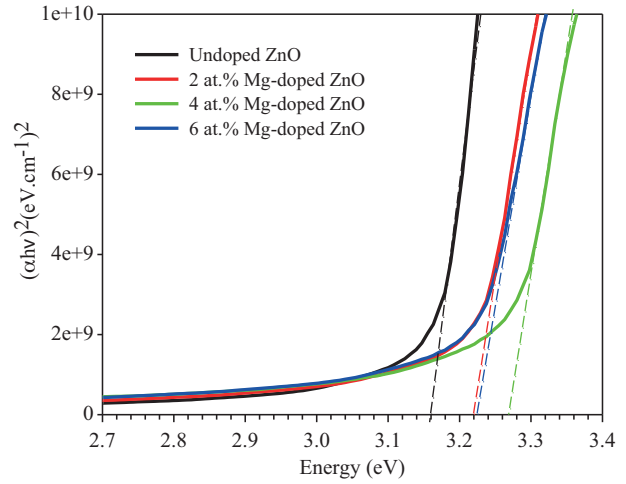
Figure 7. Tauc's plot of undoped, 2 at.%, 4 at.%, and 6 at.% Mg-doped ZnO samples.

entering more Mg atoms into the structure as well as the nonradiative recombinations induced by Mg atoms. Zhao and co-workers reported an analogous study dealing with the effects of various Mg concentrations (0, 3, 5, 8 at.%) on ZnO fibers. They found that, compared to undoped sample, 5 at.% Mg-doped ZnO fibers showed the maximum UV peak, whereas 8 at.% Mg-doping level gave rise to a decrease in the UV peak intensity [33]. In Figure 8, in addition to the UV peak, there is also a broad deep level emission (DLE) in the range of 410–800 nm for all the samples. It is well known that the DLE emission peak can be attributed to intrinsic defects such as V_{Zn} (410–420 nm), Zn_i (430–450 nm), V_o (480–510 nm), and O_i (600–800 nm) [34]. Even ZnO rods have these defects due to the nonstoichiometric formation of rods during the growth process confirmed by EDS results. Compared to ZnO, DLE band intensity reaches its maximum value at the wavelengths between 410 and 600 nm for the 2 at.% Mg-doped ZnO sample, indicating an enhancement in the number of V_{Zn}, Zn_i, and V_o defects. Additionally, a peak centered at 755 nm corresponding to the energy value of 1.64 eV could be particularly attributed to O_i defects. The intensity of this peak also increases with increasing Mg-doping concentration up to 2 at.%, suggesting that the population of this defect also increases. This increase might be also attributed to a decline in the nonradiative recombination defects as well as an enhancement in the nonradiative recombination lifetime [35]. After 4 at.% Mg doping, though the intensity of the DLE band in the range of 410–440 nm slightly enhances, DLE band intensity at the wavelength range between 440 nm and 600 nm decreases with respect to that of 2 at.% Mg doping. On the other hand, the peak intensity of red luminescence (600–800 nm) takes its maximum value. These all mean that the defect density of V_{Zn}, Zn_i, and O_i increases for 4 at.% Mg doping whereas the defect population of V_o declines. However, as for the 6 at.% Mg-doped ZnO sample, the peak intensity of the DLE band along all the spectrum decreases, which implies that the population of defects of V_{Zn}, Zn_i, V_o, and O_i decreases. This reduction may be explained by the recombination of pairs including V_o–O_i and V_{Zn}–Zn_i, causing a decline in the numbers of all these defects.

Figure 9 depicts the J–V curves of DSSCs based on undoped and Mg-doped ZnO samples and their photovoltaic characteristics are listed in Table 2. It is noted that ZnO rods have a short circuit current density (J_{sc}) of 0.111 mA/cm^2 and an open circuit voltage (V_{oc}) of 0.38 V, achieving a power conversion efficiency (η) of 0.0054%. Polat previously reported that undoped ZnO nanorod-based DSSCs prepared by CBD route displayed J_{sc} of 0.43 mA/cm^2 and V_{oc} of 0.46 V, which were higher than those produced by SP [22]. For 2 at.% Mg-doped ZnO-based DSSCs, J_{sc} and V_{oc} values greatly improve up to 0.235 mA/cm^2 and 0.45 V,
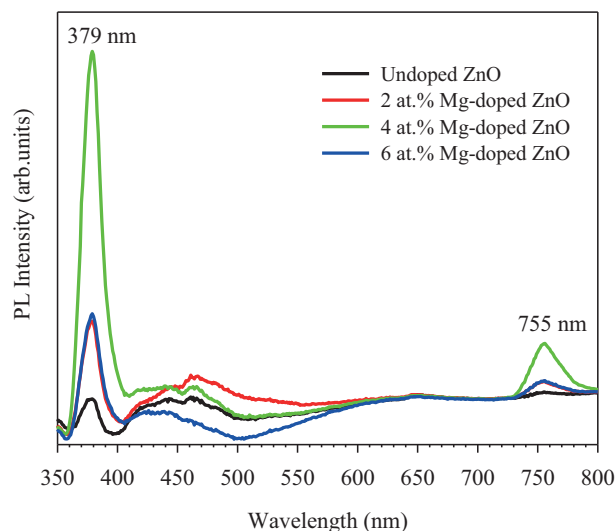
Figure 8. PL spectra of undoped, 2 at.%, 4 at.%, and 6 at.% Mg-doped ZnO samples.
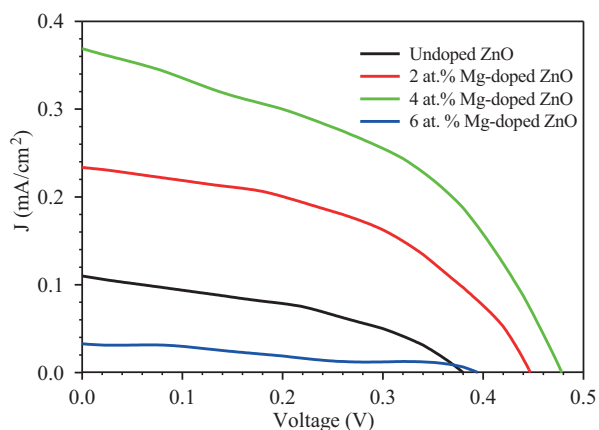

Figure 9. J–V curves of DSSCs-based Mg-doped ZnO samples ($Zn_{1-x}Mg_xO$: x = 0.0, 0.02, 0.04, 0.06) photoanode.

respectively. Thus, a corresponding solar to electricity conversion efficiency is obtained as 0.05%, which means that η value is enhanced more than 800% compared to that of the undoped one. After 4 at.% Mg doping, J_{sc} and V_{oc} take their maximum values of 0.368 mA/cm^2 and 0.48 V, respectively, and a maximum light harvesting efficiency of 0.08% is obtained. According to our published study, 4 at.% Mg-doped ZnO nanorod-based DSSCs exhibited J_{sc} of 0.43 mA/cm^2 and V_{oc} of 0.56 V, which were higher than those obtained here [24]. The rise in the overall efficiency upon 2 at.% and 4 at.% Mg doping can be attributed to the increase in both J_{sc} and V_{oc}. The increase in the J_{sc} value could be explained by the morphological change. That is, as seen in SEM results, 2 at. and 4 at.% Mg-doped ZnO samples have rougher surfaces than does ZnO, suggesting that they absorb more dye molecules, resulting in an enhancement in J_{sc}. Additionally, 2 at. and 4 at.% Mg doping could cause more efficient electron transport that might also increase the J_{sc} value [36,37]. On the other hand, after ZnO is doped with 2 at. % and 4 at.% Mg, the rise in the V_{oc} values could be correlated with the enhancement in the band gap value. It can be seen in Figure 7 that band gap values of our samples increase up to 4 at.% Mg-doping compared to ZnO and 4 at.% Mg-doped ZnO based DSSCs exhibit the best overall efficiency. Raj and co-workers reported similar work investigating the effects of Mg doping on ZnO-based DSSCs. They found that the band gap value of the ZnO sample increased with the increase in Mg-doping level up to 5 at.% and this increase in the band gap value corresponded to a rise in the power conversion efficiency of the fabricated DSSCs [23]. However, a further increase in the Mg-doping level of 6 at.% remarkably causes a reduction in J_{sc} of 0.034 mA/cm^2 and also V_{oc} value slightly decreases to 0.39 V compared to 4 at.% Mg doping. The corresponding power conversion efficiency is 0.00047%, which is the worst value obtained in this study. The reason for the minimum overall efficiency is related to the very small J_{sc} value. As discussed above, the morphological change has an important effect on J_{sc}. As seen in Figures 3d and 4d, the 6 at.% Mg-doped ZnO sample includes surfaces smoother than those of the others, which means that it does not absorb many dye molecules. Therefore, the minimum J_{sc} value is attained. In addition, the deterioration in crystal quality upon 6 at.% Mg doping, which can be easily seen from the result of XRD, could be responsible for the smallest value of J_{sc}. On the other hand, a slight decline in the V_{oc} value of 6 at.% Mg-doping level may be attributed to the decline in the band gap, which is similar to a discussion dealt with before.

Table 2. Performance of DSSCs including undoped and Mg-doped ZnO photoanodes under 100 mW/cm^2.

Photoanode	J_{sc} (mA cm^{-2})	V_{oc} (V)	$P_{\max}$ (mW/cm^2)	FF	η (%)
ZnO	0.111	0.38	0.005	0.12	0.0054
2 at.% Mg-doped ZnO	0.235	0.45	0.049	0.46	0.05
4 at.% Mg-doped ZnO	0.368	0.48	0.078	0.44	0.08
6 at.% Mg-doped ZnO	0.034	0.39	0.0044	0.33	0.00047

4. Conclusions

Undoped and Mg-doped ZnO samples used as a photoanode in DSSCs were prepared using SP on FTO substrates. From XRD and SEM, it was seen that undoped and Mg-doped ZnO samples had hexagonal structures, and the ZnO sample was composed of very compact rod morphology with hexagons. After 2 at.% Mg doping, the surface morphology significantly changed to a polyhedral rod structure. From optical measurements, it was found that ZnO rods had a transmittance of nearly 50% at the wavelength range of 550–900 nm. The band gap value (E_g) of the undoped sample was determined to be 3.16 eV and this value increased gradually up to 3.27 eV for the 4 at.% Mg-doped ZnO sample. However, after ZnO was doped with 6 at.% Mg, the band gap value decreased to 3.22 eV. RTPL experiments exhibited that all samples had three peaks: a UV emission peak (379 nm), DLE peak (410–800 nm), and a red peak (755 nm). From J–V curves, maximum conversion efficiency was calculated to be 0.08% for 4 at.% Mg-doped ZnO-based DSSCs.

References

[1] O'Regan, B.; Grätzel, M. *Nature* **1991**, *353*, 737-739.

[2] Grätzel, M. *Nature* **2001**, *414*, 338-344.

[3] Nazeeruddin, M. K.; Pechy, P.; Renouard, T.; Zakeeruddin, S. M.; Humphry-Baker, R.; Comte, P.; Liska, P.; Cevey, L.; Costa, E.; Shklover, V.; et al. *J. Am. Chem. Soc.* **2001**, *123*, 1613-1624.

[4] Chen, C.; Wang, M.; Li, J.; Pootrakulchote, N.; Alibabaei, L.; Ngocle, C.; Decopper, J.; Tsai, J.; Grätzel, C.; Wu, C.; et al. *ACS Nano.* **2009**, *3*, 3103-3109.

[5] Chen, Z.; Tang, Y.; Zhang, L.; Luo, L. *Electrochim. Acta* **2006**, *51*, 5870-5875.

[6] Kashyout, A. B.; Soliman, M.; Gamal, M. E.; Fathy, M. *Mater. Chem. Phys.* **2005**, *90*, 230-233.

[7] Lu, L.; Li, R.; Fan, K.; Peng, T. *Sol. Energy* **2010**, *84*, 844-853.

[8] Wang, Z. L. *Mater. Sci. Eng., R.* **2009**, *64*, 33-71.

[9] Yılmaz, S.; Bacaksız, E.; McGlynn, E.; Polat, İ.; Özcan, Ş. *Thin Solid Films* **2012**, *520*, 5172-5178.

[10] Lupan, O.; Guérin, V. M.; Ghimpu, L.; Tiginyanu, I. M.; Pauporté, T. *Chem. Phys. Lett.* **2012**, *550*, 125-129.

[11] Jin, C. F.; Yuan, X.; Ge, W. W.; Hong, J. M.; Xin, X. Q. *Nanotechnology* **2003**, *14*, 667-669.

[12] Kong, X.; Sun, X.; Li, X.; Li, Y. *Mater. Chem. Phys.* **2003**, *82*, 997-1001.

[13] Atuchin, V. V.; Galashov, E. N.; Kozhukhov, A. S.; Pokrovsky, L. D.; Shlegel, V. N. *J. Cryst. Growth* **2011**, *318*, 1147-1150.

[14] Motevalizadeh, L.; Shohany, B. G.; Abrishami, M. E. *Mod. Phys. Lett. B* **2016**, *30*, 1650024-1650028.

[15] Olvera, M. D. L.; Maldonado, A.; Asomoza, R. *Sol. Energy Mater. Sol. Cells* **2002**, *73*, 425-433.

[16] Rahmani, M. B.; Keshmiri, S. H.; Shafiei, M.; Latham, K.; Wlodarski, W.; du Plessis, J.; Kalantar-Zadeh, K. *Sens. Lett.* **2009**, *7*, 621-628.

[17] Kaipeng, L.; Beifang, Y.; Hongwei, Y.; Zhengping, F.; Meiwang, W.; Youjun, C.; Jian, Z. *J. Lumin.* **2009**, *129*, 969-972.

[18] Bacaksız, E.; Aksu, S.; Yılmaz, S.; Parlak, M.; Altunbaş, M. *Thin Solid Films* **2010**, *518*, 4076-4080.

[19] Mariappan, R.; Ponnuswamy, V.; Suresh, R.; Suresh, P.; Chandra Bose, A.; Ragavendar, M. *J. Alloys Compd.* **2014**, *582*, 387-391.

[20] Sahal, M.; Marí, B.; Mollar, M.; Manjón, F. J. *Phys. Status Solidi C* **2010**, *7*, 2306-2310.

[21] Yun, S.; Lee, J.; Chung, J.; Lim, S. *J. Phys. Chem. Solids* **2010**, *71*, 1724-1731.

[22] Polat, İ. *J. Mater. Sci. - Mater. Electron.* **2014**, *25*, 3721-3726.

[23] Raj, C. J.; Prabakar, K.; Karthick, S. N.; Hemalatha, K. V.; Son, M. K.; Kim, H. J. *J. Phys. Chem. C* **2013**, *117*, 2600-2607.

[24] Polat, İ.; Yılmaz, S.; Bacaksız, E.; Atasoy, Y.; Tomakin, M. *J. Mater. Sci. - Mater. Electron.* **2014**, *25*, 3173-3178.

[25] Iqbal, J.; Jan, T.; Ismail, M.; Ahmad, N.; Arif, A.; Khan, M.; Adil, M.; Sami-ul, H.; Arshad, A. *Ceram. Int.* **2014**, *40*, 7487-7493.

[26] Yılmaz, S.; Parlak, M.; Özcan, Ş.; Altunbaş, M.; McGlynn, E.; Bacaksız, E. *Appl. Surf. Sci.* **2011**, *257*, 9293-9298.

[27] Li, Z. H.; Cho, E. S.; Kwon, S. J. *Appl. Surf. Sci.* **2014**, *314*, 97-103.

[28] Ginting, R. T.; Yap, C. C.; Yahaya, M.; Salleh, M. M. *J. Alloys Compd.* **2014**, *585*, 696-702.

[29] Çaglar, M.; Çaglar, Y.; Ilican, S. *Physica B* **2016**, *485*, 6-13.

[30] Agrawal, A.; Dar, T. A.; Phase, D. M.; Sen, P. *J. Cryst. Growth* **2013**, *384*, 9-12.

[31] Abed, C.; Bouzidi, C.; Elhouichet, H.; Gelloz, B.; Ferid, M. *Appl. Surf. Sci.* **2015**, *349*, 855-863.

[32] Singh, V. P.; Rath, C. *RSC Adv.* **2015**, *5*, 44390-44397.

[33] Zhaoa, M.; Wanga, X.; Ninga, L.; Hea, H.; Jiaa, J.; Zhang, L.; Xinjian, L. *J. Alloys Compd.* **2010**, *507*, 97-100.

[34] Yılmaz, S.; McGlynn, E.; Bacaksız, E.; Cullen, J.; Chellappan, R. K. *Chem. Phys. Lett.* **2012**, *525*, 72-76.

[35] Lin, Y. J.; Wu, P. H.; Tsai, C. L.; Liu, C. J.; Lin, Z. R.; Chang, H. C.; Lee, C. T. *J. Appl. Phys.* **2008**, *103*, 113709-11373.

[36] Ye, N.; Qi, J.; Qi, Z.; Zhang, X.; Yang, Y.; Liu, J.; Zhang, Y. *J. Power Sources* **2010**, *195*, 5806-5809.

[37] Nayeri, F. D.; Soleimani, E. A.; Salehi, F. *Renewable Energy* **2013**, *60*, 246-255.